MEK-SHP2 inhibition prevents tibial pseudarthrosis caused by NF1 loss in Schwann cells and skeletal stem/progenitor cells

Simon Perrin, Sanela Protic, Vincent Bretegnier, Ingrid Laurendeau, Oriane Duchamp de Lageneste, Nicolas Panara, Odile Ruckebusch, Marine Luka, Cécile Masson, Théodora Maillard, et al.

MEK-SHP2 inhibition prevents tibial pseudarthrosis caused by *NF1* loss in Schwann cells and skeletal stem/progenitor cells

Simon Perrin[1], Sanela Protic[1], Vincent Bretegnier[1], Ingrid Laurendeau[2], Oriane Duchamp de Lageneste[1], Nicolas Panara[2], Odile Ruckebusch[3], Marine Luka[4,5], Cécile Masson[6,7], Théodora Maillard[8], Fanny Coulpier[1], Stéphanie Pannier[9], Philippe Wicart[9], Smail Hadj-Rabia[10], Katarzyna J. Radomska[1], Mohammed Zarhrate[7,11], Mickael Ménager[4,5], Dominique Vidaud[2,8], Piotr Topilko[1], Béatrice Parfait[2,8], and Céline Colnot[1,*]

[1] Univ Paris Est Creteil, INSERM, IMRB, 94000, Creteil, France

[2] INSERM UMR S1016, Institut Cochin, Université Paris Cité, 75014, Paris, France

[3] Univ Paris Est Creteil, INSERM, IMRB, Plateforme de Cytométrie en flux, 94000, Creteil, France

[4]Paris Cité University, Imagine Institute, Laboratory of Inflammatory Responses and Transcriptomic Networks in Diseases, Atip-Avenir Team, INSERM UMR 1163, 75015, Paris, France.

[5] Labtech Single-Cell@Imagine, Imagine Institute, INSERM UMR 1163, 75015, Paris, France.

[6] Bioinformatics Core Facility, Institut Imagine-Structure Fédérative de Recherche Necker, INSERM U1163, 75015, Paris, France.

[7] INSERM US24/CNRS UAR3633, Paris Cité University, 75015, Paris, France

[8] Service de Médecine Génomique des Maladies de Système et d'Organe, Hôpital Cochin, DMU BioPhyGen, Assistance Publique-Hôpitaux de Paris, AP-HP, Centre-Université Paris Cité, F-75014 Paris, France

[9] Department of Pediatric Orthopedic Surgery and Traumatology, Necker-Enfants Malades Hospital, AP-HP, Paris Cité University, 75015, Paris, France

[10] Department of Dermatology, Reference Center for Rare Skin Diseases (MAGEC), Imagine Institute, Necker-Enfants Malades Hospital, AP-HP, Paris Cité University, 75015, Paris, France.

[11] Genomics Core Facility, Institut Imagine-Structure Fédérative de Recherche Necker, INSERM U1163, 75015, Paris, France.

*Corresponding author: celine.colnot@inserm.fr

One Sentence Summary

Combined MEK-SHP2 inhibition prevents fibrotic failure to heal in a preclinical model of congenital pseudarthrosis of the tibia.

Abstract

Congenital pseudarthrosis of the tibia (CPT) is a severe pathology marked by spontaneous bone fractures that fail to heal leading to fibrous nonunion. Half of patients with CPT are affected by the multisystemic genetic disorder neurofibromatosis type 1 (NF1), caused by mutations in the *NF1* tumor suppressor gene, a negative regulator of RAS-MAPK signaling pathway. Here, we analyzed patients with CPT and *Prss56-Nf1* knockout mice to elucidate the pathogenic mechanisms of CPT-related fibrous nonunion and explored a pharmacological approach to treat CPT. We identified *NF1*-deficient Schwann cells and skeletal stem/progenitor cells (SSPCs) in pathological periosteum as affected cell types driving fibrosis. Whereas *NF1*-deficient SSPCs adopted a fibrotic fate, *NF1*-deficient Schwann cells produced critical paracrine factors including TGFβ and induced fibrotic differentiation of wild-type SSPCs. To target both *NF1*-deficient Schwann cells and SSPCs, we used combined MEK and SHP2 inhibitors to counteract the elevated RAS-MAPK signaling in human SSPCs. Combined MEK-SHP2 inhibition in vivo prevented fibrous nonunion in the *Prss56-Nf1* knockout mouse model, providing a promising therapeutic strategy for the treatment of fibrous nonunion in CPT.

Introduction

Congenital pseudarthrosis of the tibia (CPT) is a rare but severe pathology that manifests mostly in children prior to 2 years of age. Patients with CPT present with tibial bowing at birth leading to spontaneous fracture and failure to heal due to fibrous nonunion. CPT treatment is exclusively surgical and remains highly challenging, with substantial risk of re-fracture or amputation *(1, 2)*. Pharmacological treatments are needed to improve CPT management, but the pathogenic mechanisms remain poorly understood and a relevant pre-clinical model for CPT is lacking. CPT can be classified as isolated CPT of unknown etiology, or NF1-related CPT in patients diagnosed with neurofibromatosis type 1 (NF1). NF1 is one of the most common multisystemic genetic disorders that affects 1 in 3000 individuals. Patients with NF1 can exhibit a variety of symptoms, including benign nerve sheath tumors, called cutaneous and plexiform neurofibromas (NFBs), skin hyperpigmentation (Café-au-lait macules, CALMs), learning disabilities, and bone manifestations *(3)*. NF1 is caused by heterozygous mutations in the *NF1* gene encoding the tumor-suppressor neurofibromin, a negative regulator of RAS and the MAPK pathway. The diverse NF1 symptoms result from a second somatic mutational event in specific tissues and cell types. NFBs and CALMs have been shown to result from *NF1* biallelic inactivation in Schwann cells and melanocytes respectively *(4–8)*.

Although *NF1* biallelic inactivation has been reported in CPT, the specific cell types harboring *NF1* loss have not been identified. The presence of pathological periosteum suggests the involvement of the periosteum in the pathogenesis of CPT *(9–11)*. Located on the outer layer of bones, the periosteum is essential for bone regeneration and contains a major source of skeletal stem/progenitor cells (SSPCs) as well as immune, endothelial, and neural cells *(12–18)*. Until now, investigations of NF1 bone manifestations in mouse models have focused mainly on the skeletal lineage and the consequences of *Nf1* gene inactivation on fracture repair have been examined using bone-specific Cre lines *(19–23)*. However, targeting *Nf1* solely in bone lineages does not recapitulate other NF1 features. Recent work by Radomska et al. reported the *Prss56-Nf1* knockout (KO) mouse model that faithfully recapitulates several NF1 symptoms, demonstrating that *Prss56*-expressing boundary cap (BC) cells are the cellular origin of cutaneous and plexiform NFBs, as well as skin hyperpigmentation *(24)*. Located at the surface of the neural tube during development, BC cells are transient neural crest-derived populations giving rise to various derivatives in nerves and skin such as Schwann cells, fibroblasts, and melanocytes *(25)*.

The common BC origin of NF1 dermatological and neurological lesions raises the question of a common cellular origin with NF1 bone manifestations.

Pharmacological interventions for NF1-related conditions are mostly targeting the RAS-MAPK signaling pathway. Several preclinical studies demonstrated the efficacy of MEK-inhibitors to counteract the elevated RAS-MAPK signaling due to reduced neurofibromin activity in cells lacking *NF1 (26, 27)*. This led to a successful clinical trial and Food and Drug Administration (FDA) approval of selumetinib in 2020 for patients with inoperable plexiform NFBs *(27–29)*. MEK inhibitors have also been tested in animal models exhibiting bone phenotypes associated with *Nf1* loss of function in bone cells but showed limited effects *(19, 22)*. Other approaches such as BMP2, bisphosphonates, lovastatin, and beta-catenin inhibition have also shown variable results *(19, 30–32)*.

This study aimed to identify the cellular origin and pathogenic mechanisms of CPT to develop efficient therapeutic strategies. Combined analyses of samples from patients with CPT and from the *Prss56-Nf1* KO mouse model unraveled the conserved mechanisms of CPT between mice and humans. We performed genetic analyses of patient pseudarthrosis tissues to search for *NF1* second hit mutations in various cell types in the periosteum including SSPCs and Schwann cells. To elucidate the role of RAS-MAPK pathway overactivation in CPT, we investigated the tibial pseudarthrosis phenotype of *Prss56-Nf1* KO mice that carry *Nf1* gene inactivation in BC derived SSPCs and Schwann cells in periosteum. Based on these results, we posited that combining MEK with SHP2 inhibition would drive robust responses in NF1 bone lesions, as SHP2 is a master positive regulator of RAS-MAPK pathway upstream of RAS *(33, 34)*. We tested the efficacy of combined MEK and SHP2 inhibition to prevent pseudarthrosis in the pre-clinical *Prss56-Nf1* KO mouse model.

Results

SSPCs and Schwann cells within pathological periosteum carry *NF1* biallelic inactivation in CPT

To investigate the tissue specificity of *NF1* biallelic inactivation in CPT, we performed *NF1* targeted sequencing of tissues from the affected pseudarthrosis (PA) site, the unaffected iliac crest (IC), and blood of 17 patients undergoing surgical treatment (Figure 1A-B, Table S1). We detected *NF1* biallelic inactivation primarily in the periosteum of the PA site (13/17 patients, Figure 1C). We also identified *NF1* biallelic inactivation in fibrous tissue (6/17 patients), bone (6/17) and bone marrow (4/17) at the PA site and in skeletal muscle (3/14) and skin (2/14) adjacent to the PA site. *NF1* biallelic inactivation was not detected in blood or IC. Of note, 2 *NF1* hits were detected in patients with NF1-related CPT as well as patients with isolated CPT, revealing that most CPTs are caused by *NF1* loss of function (Figure 1D). We observed the same *NF1* second hit in tibia and fibula in 4/5 patients affected by combined tibia and fibula CPT (Figure S1A). Moreover, in 3 patients, we identified the same *NF1* second hit in PA periosteum, muscle and skin surrounding the PA site (Figure S1B). These results indicate that the second mutational event occurred during early skeletogenesis and was not restricted to the skeletal lineage. Next, we sought to identify the cell types carrying *NF1* biallelic inactivation in the periosteum. We detected 2 *NF1* hits in cultured periosteal SSPCs (pSSPCs) from 9 of the 13 patients carrying 2 hits in the periosteum (Figure 1E, Table S1). Thus, pSSPCs carry *NF1* biallelic inactivation but are not the only affected cell type. We then performed droplet digital PCR on sorted cell populations from PA periosteum of patient P15 (Figure S1C-G). The same *NF1* variants were detected in SSPCs and in Schwann cells, but not in endothelial or immune cells (Figure 1F, Figure S1E). This revealed that Schwann cells also carry *NF1* biallelic inactivation in CPT, and that mutated pSSPCs and Schwann cells in P15 are derived from a common lineage. *NF1* inactivation in periosteum led to an increased percentage of pERK+ cells in PA compared to IC periosteum (Figure 1G). Co-immunostaining of pERK and specific cell markers correlated with the genetic results as we observed the presence of increased percentage of pERK+CD90+ SSPCs and pERK+SOX10+ Schwann cells in PA periosteum compared to IC periosteum, but not of pERK+CD31+ endothelial cells, pERK+CD68+ immune cells, or pERK+αSMA+ pericytes/smooth muscle cells (Figure 1H). The percentages of pERK+ SSPCs and Schwann cells at PA site were correlated, suggesting the presence of both mutated cell types in all patients (Fig. S1H). Overall, the results show that SSPCs and Schwann cells within periosteum are the cell types carrying *NF1* biallelic inactivation in CPT and that mutated pSSPCs and Schwann cells share a common origin.

_Nf1_ inactivation in BC-derived pSSPCs and Schwann cells cause tibial pseudarthrosis in mice

To explore the role of SSPCs and SCs in CPT, we analyzed the *Prss56-Nf1 KO* mouse model *(24)*. Lineage tracing analyses in *Prss56^{Cre}; R26^{tdTom}* mice showed that BC-derived tdTom+ cells are a rare cell population in adult bone found predominantly within the periosteum in uninjured tibia and correspond to Platelet-Derived Growth Factor Receptor α+ (PDGFRα+) SCA1+ pSSPCs and SOX10+ Schwann cells (Figure 2A, Figure S2-S3). Analyses from developmental stages to adulthood showed that *Prss56* expression was not detected in bone, indicating the BC-origin of tdTom+ SSPCs and SCs in the periosteum of *Prss56^{Cre}; R26^{tdTom}* mice (Figure S4). To determine if *Prss56-Nf1* KO mice exhibit congenital pseudarthrosis, we analyzed their bone parameters and induced tibial fracture in 3-month-old *Prss56^{Cre}; R26^{tdTom}; Nf1$^{fl/fl}$ (Prss56-Nf1$^{fl/fl}$)* and *Prss56^{Cre}; R26^{tdTom}; Nf1$^{fl/-}$ (Prss56-Nf1$^{fl/-}$)* mutant mice, and *Prss56^{Cre}; R26^{tdTom}; Nf1$^{+/+}$ (Prss56-Nf1$^{+/+}$)* controls. Although we only detected a mild reduction in tibial length of uninjured tibia (Figure S5), we observed a severe reduction in callus and bone volumes in both *Prss56-Nf1$^{fl/fl}$* and *Prss56-Nf1$^{fl/-}$* mutant mice through all stages of bone repair, as well as delayed cartilage formation and resorption (Figure S6A-B). From day 14 post-fracture, we observed persistence of fibrotic tissue in the callus (Figure 2B, Figure S6A). Absence of bone bridging was striking 28 days post-fracture on microCT scans of *Prss56-Nf1$^{fl/fl}$* and *Prss56-Nf1$^{fl/-}$* mutant calluses and correlated with fibrotic accumulation (Figure 2C-D, Figure S6). The percentage of bone union was significantly different between mutant and control mice (p=0.0067) but not between the mutant groups (p=0.52). We confirmed the fracture nonunion phenotype of *Prss56-Nf1* KO mice using a semi-stabilized fracture model (Figure S7). Thus, *Nf1* biallelic inactivation in BC-derived pSSPCs and SCs leads to tibial pseudarthrosis.

_Nf1_-deficient BC-derived pSSPCs and Schwann cells contribute to callus fibrosis

We then investigated the identity and fate of BC derivatives in uninjured tibia and fracture callus of *Prss56-Nf1$^{+/+}$* and *Prss56-Nf1$^{fl/f}$* mice. We observed an increased percentage of tdTom+ periosteal cells in *Prss56-Nf1$^{fl/f}$* mice compared to control mice, likely due to their increased proliferation. At 14 days post-injury, tdTom+ cells were heterogeneously distributed in the fracture callus with regions rich in tdTom+ cells and regions without tdTom+ cells (Figure S8A-B). In *Prss56-Nf1$^{+/+}$* control mice, tdTom+ cells were SOX9+ cartilage cells and OSX+ bone cells but their contribution to cartilage was decreased

in *Prss56-Nf1*$^{fl/fl}$ mice (Figure 2E-F, Figure S8C-D). TdTom+ cells were localized in POSTN+ fibrotic tissue of *Prss56-Nf1*$^{fl/fl}$ calluses and corresponded to SOX10+ Schwann cells and *Postn*-expressing fibroblastic cells (Figure 2G, Figure S8E). TdTom+ Schwann cells in callus fibrosis presented a repair Schwann cell phenotype as they were positive for the stemness marker SOX2, were negative for the differentiation marker Myelin Basic Protein (MBP) and were not localized along nerves (Figure 2G). Although we detected tdTom+ fibrotic cells, the fibrous tissue of *Prss56-Nf1*$^{fl/fl}$ calluses was mostly composed of non-traced cells, indicating that wild-type cells also contributed to callus fibrosis (Figure S8E). This correlated with NGS results from patient samples, where we observed absence or low percentage of *NF1*-mutated cells in PA fibrous tissue whereas a high percentage of *NF1* mutated cells was detected in PA periosteum (Table S2). Hence, *Nf1*-deficient SSPC and SCs from the periosteum, as well as wild-type cells contribute to callus fibrosis in CPT.

_NF1_-deficient periosteal SSPCs adopt a fibrotic fate during bone repair

To explore the impact of *NF1* biallelic loss on the periosteum and pSSPCs, we compared PA periosteum from patients P5 and P13 with IC periosteum from patients P13 and P15 using single-nucleus RNAseq (snRNAseq) analyses (Figure 3A, Figure S9A-D). We identified 4 main cell populations: pericytes/smooth muscle cells (SMCs), endothelial cells, immune cells, and SSPCs/fibroblasts encompassing three subpopulations expressing *PDGFRA*, *ADAM12/NCAM1* (CD56), and osteochondral genes (Figure 3B-C, Figure S9D). The percentage of SSPCs/fibroblasts and *ADAM12*+ cells was increased in periosteum from PA site (Figure 3D). In addition, PA periosteum displayed increased fibrotic, osteogenic, chondrogenic, and cellular responses to TGFβ lineage scores compared to IC periosteum, revealing the pro-fibrotic phenotype of pSSPCs in PA periosteum (Figure 3E). We also observed increased MAPK activation lineage score in PA periosteum, correlated with biallelic *NF1* loss detected in this tissue. We performed bulk RNAseq analyses of IC and PA primary pSSPCs carrying *NF1* biallelic inactivation and MAPK overactivation (Figure S10E). We confirmed the pro-fibrotic phenotype of PA pSSPCs, which overexpressed fibrotic and MAPK-related genes and were enriched for Gene Ontology related to skeletal development and extracellular matrix (ECM) (Figure S10F-G). We observed increased proliferation and impaired in vitro chondrogenic differentiation (5/6 patients) of PA compared to IC pSSPCs (Figure S10H-I) and detected variable effect of *NF1* biallelic inactivation on the osteogenic and adipogenic differentiation of pSSPCs (Figure S10I). To investigate the impact of *NF1*

loss of function on the regenerative potential of pSSPCs, we grafted PA- or IC-derived pSSPCs at the fracture site of immunodeficient mice (Figure 3F, Figure S10J). PA-derived pSSPCs switched from a chondrogenic to a fibrotic fate after fracture as they were detected within fibrotic tissue, whereas IC-derived pSSPCs mostly contributed to cartilage in the fracture callus (Figure 3G). The pro-fibrotic fate of PA-derived pSSPCs led to an increase of total callus fibrosis and altered bone healing at 28 days post-injury (Figure 3H). We also observed the fibrotic fate of *Nf1*-deficient pSSPCs in *Prss56-Nf1* KO mice. We grafted periosteum or cultured pSSPCs from *Prss56-Nf1*$^{fl/fl}$ mutant or *Prss56-Nf1*$^{+/+}$ control mice at the fracture site of wild-type hosts (Figure 3I, Figure S11A-G). Although the contribution to the callus was equivalent (Figure S11H), we observed a reduced contribution to cartilage of mutant compared to control tdTom+ periosteum or pSSPCs. These tdTom+ mutant cells were present in callus fibrosis, indicating a fate change of *Nf1*-deficient pSSPCs during bone repair (Figure 3I). In sum, *NF1* biallelic inactivation causes fibrotic differentiation of pSSPCs in response to bone fracture.

Fibrotic differentiation of *Nf1*-deficient pSSPCs is due to over activation of MAPK pathway

To uncover the molecular mechanisms underlying pSSPC fate conversion, we first investigated the role of the MAPK pathway during the early response of pSSPCs to bone fracture. We analyzed snRNAseq datasets from uninjured periosteum, and from injured periosteum and hematoma/callus at days 3, 5 and 7 post-fracture in wild-type mice *(16)* (Fig 4A). SSPCs activate in 3 successive phases: a stem/progenitor phase predominant in the uninjured dataset, an injury-induced fibrogenic phase predominant at day 5 post-fracture, and a bifurcation between osteogenesis and chondrogenesis, predominant at day 7 post-fracture (Figure 4B). We assessed the MAPK pathway activation during these 3 phases using a MAPK score based on the expression profile of MAPK target genes. Along pseudotime, we observed an increase of MAPK score between the SSPC and fibrogenic stages, followed by a decrease when cells engage into osteochondral lineage (Figure 4C). MAPK score was reduced in cells with high chondrogenic lineage score and *Sox9* expression but remained constant in cells with a high osteogenic lineage score (Figure 4D). This showed that pSSPCs specifically downregulate the MAPK pathway to transition from the fibrogenic to the chondrogenic stage. Co-immunostaining for the chondrogenic marker SOX9 and pERK on day 7 wild-type callus sections confirmed a negative correlation between SOX9 and pERK signals (Figure 4E). Analyses in tdTom+ cells showed higher pERK and reduced SOX9 signals in *Prss56-Nf1*$^{fl/fl}$ compared to *Prss56-Nf1*$^{+/+}$

calluses. In tdTom+ *Prss56-Nf1*$^{+/+}$ cells, we observed a negative correlation between pERK and SOX9 signals whereas tdTom+ *Prss56-Nf1*$^{fl/fl}$ cells only exhibited high pERK and low SOX9 signals (Figure 4F). The fibrotic fate of *Nf1*-deficient pSSPCs is therefore caused by overactivation of MAPK signaling, which prevents the transition from fibrogenic to chondrogenic stage required for callus formation.

_Nf1_-deficient Schwann cells are the main driver of fibrosis in CPT

Because the fibrotic tissue at the pseudarthrosis site was also composed of wild-type cells in both patients with CPT and *Prss56-Nf1 KO* mice, we explored the role of the mutant fracture environment on SSPC fate. Transplanted wild-type GFP+ pSSPCs became fibrotic in the callus of *Prss56-Nf1*$^{fl/fl}$ but not *Prss56-Nf1*$^{+/+}$ hosts (Figure S11I), showing the pro-fibrotic influence of the mutant callus environment. We investigated the role of *Nf1*-deficient pSSPCs and SCs in this deleterious paracrine effect. Although transplanted *Nf1*-deficient pSSPCs induced callus fibrosis in wild-type hosts, this fibrotic tissue was resorbed, and bone bridging was apparent by 28 days post-fracture (Figure S11F-G). In contrast, transplantation of *Nf1*-deficient Schwann cells at the fracture site of wild-type hosts induced tibial pseudarthrosis with absence of bone bridging and fibrous accumulation at both 14 and 28 days post-fracture (Figure 5A). *Nf1*-deficient Schwann cells are therefore the main driver of fibrotic accumulation in tibial pseudarthrosis. We generated snRNAseq datasets of day 7 post-fracture periosteum and callus of *Prss56-Nf1*$^{fl/fl}$ mice and performed integration with day 7 control dataset (Figure 5B, Fig S12A-D). Given the rarity of tdTom+ cells, *Prss56-Nf1*$^{fl/fl}$ dataset was composed solely of non-traced (i.e., wild-type) cells in mutant environment (Figure S12E). We observed a reduced proportion of cells in chondrogenic clusters and increased proportion of cells in fibrogenic clusters in mutant compared to control dataset (Figure 5C-D). This indicated that wild-type pSSPCs in the mutant environment are partly retained in the fibrogenic stage.

We sought to identify the factors driving the pro-fibrotic effect of *Nf1*-deficient Schwann cells on SSPCs. We observed that tdTom+ Schwann cells in the fibrotic tissue of *Prss56-Nf1*$^{fl/fl}$ mice expressed *Tgfb1*, Oncostatin M (*Osm*) and *Pdgfa* (Fig. 5E), factors previously shown to be secreted by repair SCs during tissue repair *(35, 36)*. In depth analyses of cluster 6 from the snRNAseq data, corresponding to pSSPCs transitioning from the fibrogenic to the chondrogenic stage, showed an upregulation of GO terms related to TGFβ specifically in *Prss56-Nf1*$^{fl/fl}$ dataset (Figure S13). This correlated with increased *Tgfb1* expression and an increased percentage of phospho-SMAD2 (TGFβ downstream effector)-positive cells

256 in day 7 *Prss56-Nf1*$^{fl/fl}$ compared to *Prss56-Nf1*$^{+/+}$ calluses (Figure 5F-G). To confirm the role of TGFβ
257 in the pro-fibrotic effect of *Nf1*-deficient Schwann cells, we treated wild-type mice grafted with tdTom+
258 *Prss56-Nf1*$^{fl/fl}$ Schwann cells or *Prss56-Nf1*$^{fl/fl}$ mice with TGFβ blocking antibody (Figure 5H). We
259 observed decreased fibrosis in the callus of treated compared to control mice. *Prss56-Nf1*$^{fl/fl}$ mice treated
260 with TGFβ blocking antibody exhibited bone bridging and improved union score at day 28 post-fracture
261 (Figure 5I), indicating that TGFβ is one of the factors mediating the pro-fibrotic effect of *Nf1*-deficient
262 Schwann cells in tibial pseudarthrosis.
263
264 **Combined MEK and SHP2 inhibition prevents tibial pseudarthrosis**
265 To develop therapeutic approaches for CPT, we aimed to reduce the pro-fibrotic effects of *NF1* mutant
266 pSSPCs and SCs by inhibiting RAS-MAPK overactivation. We tested the efficacy of MEK inhibition using
267 selumetinib, SHP2 inhibition using SHP099, and the combination of MEK and SHP2 inhibitors to block
268 RAS-MAPK overactivation and prevent CPT. We first tested the impact of MEK with or without SHP2
269 inhibition on MAPK activation in *NF1*-deficient pSSPCs from patients with CPT. We observed a
270 substantial reduction of MAPK activation from 1 µM with combined treatment but not with single
271 treatment compared to DMSO-treated cells (Fig 6A-B). Combined MEK-SHP2 inhibition significantly
272 reduced in vitro proliferation and increased chondrogenic differentiation of *NF1*-deficient pSSPCs
273 compared to DMSO-treated cells (Figure 6C-D). As *Prss56-Nf1 KO* mice faithfully recapitulate the bone
274 repair defect observed in CPT, we tested the benefit of MEK-SHP2 inhibition on this relevant preclinical
275 model of CPT by treating daily *Prss56-Nf1*$^{fl/-}$ mice with selumetinib, SHP099, combined selumetinib and
276 SHP099, or vehicle (Figure 6E). Whereas control mice did not show bone union, mice treated with
277 combined selumetinib and SHP099 displayed an 83% union rate (Figure 6F-G), demonstrating
278 treatment efficacy in preventing pseudarthrosis. Selumetinib treatment alone had a mild effect on union
279 rate and SHP099 treatment alone was not as efficient as combined treatment (25% and 60% of union
280 rate respectively, Figure 6G). Combined MEK-SHP2 inhibition was the only treatment leading to
281 increased callus, cartilage, and bone formation and reduced fibrosis accumulation (Figure 6H).
282 Furthermore, analysis of tdTom+ cells in the fracture callus showed that combined treatment corrects
283 *Nf1*-deficient cell fate impairment, as tdTom+ cells formed cartilage instead of fibrosis in *Prss56-Nf1*
284 mutant mice treated with both SHP099 and selumetinib compared to untreated mutant mice (Figure 6I).
285 We confirmed that the combined treatment was also efficacious in the *Prx1-Nf1* KO model, in which the

pseudarthrosis phenotype results from *Nf1* inactivation in all pSSPCs (Fig. S14). Overall, combined MEK-SHP2 inhibition efficiently prevented fibrous accumulation and pseudarthrosis, demonstrating its promising therapeutic potential.

Discussion

In this study, we uncover the cellular origin and underlying molecular mechanisms of CPT, demonstrating that SSPCs and Schwann cells are the affected cell types in CPT. We detected *NF1* biallelic inactivation in SSPCs and Schwann cells and increased numbers of pERK+ SSPCs and Schwann cells in pathological periosteum of patients with CPT. These findings correlate with the presence of *Nf1*-deficient SSPCs and Schwann cells in the periosteum and fibrous callus of *Prss56-Nf1 KO* mice that exhibit tibial pseudarthrosis. Functionally, human and murine *NF1*-deficient pSSPCs in both *Prss56-Nf1* KO and *Prx1-Nf1* KO mouse models displayed a pro-fibrotic phenotype and contributed to callus fibrosis. The role of MAPK signaling in regulating SSPC differentiation is unclear, as previous studies showed beneficial and deleterious effect of MAPK cascade in chondrogenesis *(37–42)*. Using snRNAseq, we established the temporal dynamics of MAPK signaling required during pSSPC activation and differentiation in response to fracture. MAPK signaling is first up-regulated in pSSPCs that transition from a stem/progenitor stage to an injury-induced fibrogenic stage and is down-regulated during the transition from fibrogenesis to chondrogenesis. These results provide the molecular mechanism explaining the retention of *NF1*-deficient pSSPCs in the fibrogenic state as they fail to downregulate MAPK signaling due to *NF1* loss of function. Consequently, fibrotic pSSPCs accumulate in the center of the callus and interfere with fracture consolidation. These results may have a broader impact in understanding other fibrotic bone repair disorders sharing similar mechanisms with CPT.

Most strikingly, we demonstrate that *NF1* biallelic inactivation in CPT is not restricted to the skeletal lineage. Our results highlight the pivotal role of Schwann cells (SCs), a neural cell type, in promoting callus fibrosis in CPT. We identified *NF1*-deficient SCs as the source of pro-fibrotic factors causing tibial pseudarthrosis in *Prss56-Nf1 KO* mice. Although *Nf1*-deficient pSSPCs exert a pro-fibrotic effect, SCs are the main fibrotic drivers in CPT recruiting wild type pSSPCs to contribute also to callus fibrosis. SCs in the fibrous callus of *Prss56-Nf1 KO* mice exhibit a repair SC phenotype. Previous studies showed that MAPK pathway regulates the transition from SCs to repair SCs suggesting that *Nf1*-deficient SCs are blocked in a repair SC state and maintain the secretion of pro-fibrotic factors in CPT *(43–45)*. We identified that *Nf1*-deficient SCs express several profibrotic factors including TGFβ, OSM, and PDGF-AA and that inhibiting TGFβ improved healing in *Prss56-Nf1 KO* mice. This study provides evidence that SCs can interfere with the repair process of non-peripheral nervous tissues and promote fibrotic

tissue accumulation. Whereas previous studies highlighted the key paracrine role of SCs in skin and digit tip regeneration, the involvement of SCs and peripheral nerves in tissue repair dysfunctions and fibrotic disorders remains understudied *(35, 36, 46)*.

The involvement of both pSSPCs and SCs in CPT reveals mechanisms for NF1 bone manifestations. CPT and other NF1 bone phenotypes have been investigated independent of other NF1 symptoms, presumably because the cell types involved have distinct embryonic origins. SCs and melanocytes, responsible for NFBs and CALMs, are neural crest-derived, whereas axial and appendicular bones are derived from the mesoderm. Our genetic analysis of the *NF1* mutational landscape in CPT revealed that *NF1* 2nd hit occurs early during embryonic development and is not restricted to the skeletal lineage. In addition, we detected the same 2 *NF1* hits in SSPCs and SCs in pathological periosteum of one patient with CPT, showing that both affected cell types share a common origin. In mice, we identified BCs as a population giving rise to SCs and pSSPCs in long bones and showed that *Nf1* loss in these derivatives cause pseudarthrosis. This shows that BCs are the cellular origin of CPT in mice, and presumably in NF1 patients. The *Prss56-Nf1 KO* model is the first relevant model to faithfully recapitulate the variability of NF1 symptoms, demonstrating that CPT shares a common BC origin with NFBs and CALMs *(24)*. In addition to sharing a common cellular origin, we further reveal that CPTs and NFBs share common pathogenic mechanisms. In NFBs, *Nf1*-deficient SCs also secrete profibrotic factors, including TGFβ and SCF, to promote fibroblast accumulation and proliferation involved in tumor progression *(47–49)*. Our study thus highlights the parallels between NF1 symptoms and calls for more integrated analysis of NF1 features.

Beside unraveling the pathogenic bases of CPT, we demonstrate the relevance of the *Prss56-Nf1* KO mouse model as a preclinical model for CPT-related fibrous nonunion. Because NF1 symptoms share common pathogenic mechanisms, we considered therapeutical strategies developed for tumoral manifestations and showed that they can also be considered for CPT treatment. Selumetinib is FDA-approved for inoperable neurofibroma yet did not reveal substantial effects in previous mouse models of NF1 bone manifestations *(19, 32, 50)*. Therefore, we tested the combination of MEK and SHP2 inhibitors to counteract the pro-fibrotic effects of *NF1*-deficient pSSPCs and SCs. We observed a therapeutic effect of the selumetinib/SHP099 combination with efficient MAPK inhibition in *NF1*-deficient

pSSPCs and restoration of the in vitro proliferation and differentiation potential of human pSSPCs. In vivo treatment of *Prss56-Nf1* KO or *Prx1-Nf1* KO mice showed promising results, with bone union reached in 83% and 100% of callus respectively, concomitant with a drastic decrease in fibrotic accumulation one month after fracture. The effect of a 10-day oral treatment opens the door to clinical strategies for CPT overcoming potential tolerability issues of combining SHP2 and MEK inhibitors. In addition, the possibility of using local delivery to minimize these issues could also be tested. These results represent a potential breakthrough in improving the prognosis for CPT patients.

There are limitations to this study. CPT is extremely rare (1/150 000 individuals) and patients undergo surgical treatment at a young age (first surgery at 3.1 ± 1 years-old). Thus, obtaining periosteum samples of patients with CPT is challenging and only small amounts of tissues can be collected. This strongly limits our ability to isolate rare cell populations, including SCs, for extensive analysis. Similarly, in *Prss56-Nf1* KO mice, BC derivatives represent a rare subset of cells in intact periosteum and in the callus after fracture. This highlights the strong paracrine effect of *Nf1*-deficient cells but makes it challenging to isolate BC-derived cells to further explore the impact of *Nf1* loss of function in these cells. Last, the Prss56-Nf1 KO mouse model recapitulates the fibrous nonunion phenotype, but not congenital tibial bowing, which might suggest independent mechanisms and require further studies.

Materials and Methods

Study design

In our study, we aimed to understand the mechanisms causing CPT. We combined the analyses of samples from patients undergoing surgery for CPT with the analyses of the relevant *Prss56-Nf1* KO mouse model. For the human cohort, we collected tissues from patients operated for CPT at Necker-Enfants Malades hospital during this study and formal consent was obtained. For each patient, the affected PA tissue was compared with non-affected IC tissue. Two patients undergoing reintervention were excluded from the cohort as original PA tissues from the first resection were not accessible and we did not detect *NF1* biallelic inactivation. Therefore, we could not conclude on the presence/absence of *NF1* mutation. For the mouse study, all animals used for the study were included except samples with distal or proximal fractures that can affect bone repair. No outliers were excluded from the study. Based on our previous publications *(12, 13, 51)*, groups of 3 to 7 samples are sufficient to assess statistical differences between groups. The n for individual experiments is indicated in the figure legends. Every group is composed of samples from at least 2 independent experiments. For both human and mouse studies, samples were assigned a unique sample number for blinded analyses. No randomization methods were used for the study, as groups were homogeneous and composed of equivalent animals based on gender, age, and genotype.

Human tissue sample collection

Cohort and ethical approval

Sample collection from patients affected by congenital pseudarthrosis of the tibia (CPT) was performed at Necker-Enfants Malades Hospital, Paris. This study was approved by the Ethics Committee CPP-IDF-2 (#ID-RCB/EUDRACT: 2014- A01420-47; IMNIS2014-03). Informed consent of legal representatives of patients was obtained prior to sample collection. The cohort was composed of 17 patients, 7 diagnosed with NF1-associated CPT and 10 with isolated CPT. NF1 diagnosis was performed by the Dermatology department at Necker-Enfants Malades Hospital, following guidelines from International Consensus Group on Neurofibromatosis Diagnostic Criteria. Isolated CPT was defined by the absence of additional NF1 clinical feature and the absence of *NF1* pathogenic variant in blood sample. 14 patients were treated for the first time (named “Primary” operation in Table S1) and 3

were undergoing additional surgery following initial treatment (named “Reintervention”). Detailed information about patient age, gender, NF1 diagnosis, type of operation and affected bones are reported in Table S1.

Sample collection

Tissues were collected during CPT treatment surgery using the induced membrane technique typically performed in 2 steps *(52)*. The first surgical procedure consists of pseudarthrosis tissue resection, intramedullary nailing, and insertion of a cement spacer to fill the gap. During this procedure, affected periosteum, bone marrow, bone, fibrous tissue, muscle, and skin from the PA site were collected. For patients undergoing surgery as secondary treatment, the primary pseudarthrosis tissues were unavailable but were collected adjacent to the primary PA site when possible. After 6 to 8 weeks, a second surgical procedure was performed to remove the cement spacer and graft autologous iliac crest periosteum and cancellous bone in the induced membrane that formed around the cement. During this second procedure, unaffected periosteum and spongy bone from the iliac crest (IC) were harvested. A blood sample was also collected during surgery. Tissue dissection and identification was performed by orthopedic surgeons. Collected tissues were immediately placed in DMEM (21063029, ThermoFischer Scientific) with 10% HEPES (15630056, ThermoFischer Scientific) and 1% Penicillin-Streptomycin (15140122, ThermoFischer Scientific) at 4°C, and processed for *NF1* genotyping, single-nuclei RNAseq, primary culture and histological analyses as described below.

Mice

C57BL/6ScNj, *Prx1*^{Cre} (IMSR_JAX:005584) *(53)*, *Rosa26-mtdTomato-mEGFP* (*R26*^{mTmG}) (IMSR_JAX:007676) *(54)*, *R26tdTomato* (*R26*^{tdTom}) (IMSR_JAX:007914) *(55)*, *Nf1*^{flox} (*Nf1*^{fl}) (IMSR_JAX:017640), *Nf1*-knock out (*Nf1*$^{-}$) *(56)* were obtained from Jackson Laboratory. *Prss56*^{Cre} mice were generated by Piotr Topilko *(24, 25)*. Immunodeficient nude CD1 mice were purchased from Janvier Labs. Mice were bred in animal facilities at IMRB, Creteil and Imagine Institute, Paris. Two to five mice were kept in separated ventilated cages, in a pathogen-controlled environment with 12:12-hour light:dark cycles and ad libitum access to water and food. All procedures performed were approved by Paris University or Paris Est Creteil University Ethical Committees (#2795-201506051048131, #19295-2019052015468705, #27181-202009141201846, #33818-2021110818301267). Males and females

were mixed in experimental groups. No specific randomization method was used. Bone injury and tissue collection for graft and digestion were performed on 10- to 14-week-old mice. Six- to 8-week-old mice were used for primary periosteum culture. Controlled breeding was performed to collect embryonic tissues at 12.5, 13.5, and 14.5 days of development. Samples were labeled at the time of tissue collection and using a labeling system allowing blind analyses in all experiments.

Statistical analyses

Data are reported as mean +/- standard deviation. n represents the number of samples used for the analysis. For human experiments, each sample corresponds to a different patient. For mouse experiments, each sample corresponds to an individual mouse. Statistical differences between experimental groups were evaluated using GraphPad Prism. For comparison between 2 groups, two-side Mann-Whitney test was used. For comparison between 3 or 4 groups, one-way ANOVA followed by Holm-Šídák's multiple comparisons post-hoc test was used. The comparison in bone bridging between mutants and control groups was performed using Chi-squared test. For SOX9/pERK signal correlation, each value corresponds to an individual cell. Correlation analysis and simple linear regression were performed to assess the correlation between both signals. Significance was determined as *$p < 0.05$, **$p < 0.01$, ***$p < 0.001$, ****$p < 0.0001$. All experiments were performed in at least 2 independent experiments.

List of Supplementary Materials

Material and Methods
Figure S1 to Figure S14
Table S1 to Table S6
MDAR checklist
Data File S1

References

1. S. Pannier, Congenital pseudarthrosis of the tibia. *Orthopaedics & Traumatology: Surgery & Research* **97**, 750–761 (2011).

2. M. J. Siebert, C. A. Makarewich, Anterolateral Tibial Bowing and Congenital Pseudoarthrosis of the Tibia: Current Concept Review and Future Directions. *Curr Rev Musculoskelet Med* **15**, 438–446 (2022).

3. D. H. Gutmann, R. E. Ferner, R. H. Listernick, B. R. Korf, P. L. Wolters, K. J. Johnson, Neurofibromatosis type 1. *Nat Rev Dis Primers* **3**, 17004 (2017).

4. I. Eisenbarth, G. Assum, D. Kaufmann, W. Krone, Evidence for the presence of the second allele of the neurofibromatosis type 1 gene in melanocytes derived from café au laitmacules of NF1 patients. *Biochem Biophys Res Commun* **237**, 138–141 (1997).

5. L. Kluwe, R. Friedrich, V. F. Mautner, Loss of NF1 allele in Schwann cells but not in fibroblasts derived from an NF1-associated neurofibroma. *Genes Chromosomes Cancer* **24**, 283–285 (1999).

6. L. Q. Le, C. Liu, T. Shipman, Z. Chen, U. Suter, L. F. Parada, Susceptible stages in Schwann cells for NF1-associated plexiform neurofibroma development. *Cancer Res* **71**, 4686–4695 (2011).

7. J. Wu, J. P. Williams, T. A. Rizvi, J. J. Kordich, D. Witte, D. Meijer, A. O. Stemmer-Rachamimov, J. A. Cancelas, N. Ratner, Plexiform and dermal neurofibromas and pigmentation are caused by Nf1 loss in desert hedgehog-expressing cells. *Cancer Cell* **13**, 105–116 (2008).

8. Y. Zhu, P. Ghosh, P. Charnay, D. K. Burns, L. F. Parada, Neurofibromas in NF1: Schwann cell origin and role of tumor environment. *Science* **296**, 920–922 (2002).

9. B. Hermanns-Sachweh, J. Senderek, J. Alfer, B. Klosterhalfen, R. Büttner, L. Füzesi, M. Weber, Vascular changes in the periosteum of congenital pseudarthrosis of the tibia. *Pathol Res Pract* **201**, 305–312 (2005).

10. D. A. Stevenson, H. Zhou, S. Ashrafi, L. M. Messiaen, J. C. Carey, J. L. D'Astous, S. D. Santora, D. H. Viskochil, Double inactivation of NF1 in tibial pseudarthrosis. *Am J Hum Genet* **79**, 143–148 (2006).

11. C. Brekelmans, S. Hollants, C. De Groote, N. Sohier, M. Maréchal, L. Geris, F. P. Luyten, L. Ginckels, R. Sciot, T. de Ravel, L. De Smet, J. Lammens, E. Legius, H. Brems, Neurofibromatosis type 1-related pseudarthrosis: Beyond the pseudarthrosis site. *Hum Mutat* **40**, 1760–1767 (2019).

12. O. Duchamp de Lageneste, A. Julien, R. Abou-Khalil, G. Frangi, C. Carvalho, N. Cagnard, C. Cordier, S. J. Conway, C. Colnot, Periosteum contains skeletal stem cells with high bone regenerative potential controlled by Periostin. *Nat Commun* **9**, 773 (2018).

13. A. Julien, S. Perrin, E. Martínez-Sarrà, A. Kanagalingam, C. Carvalho, M. Luka, M. Ménager, C.

Colnot, Skeletal stem/progenitor cells in periosteum and skeletal muscle share a common molecular response to bone injury. *J of Bone & Mineral Res* , jbmr.4616 (2022).

14. Z. Li, C. A. Meyers, L. Chang, S. Lee, Z. Li, R. Tomlinson, A. Hoke, T. L. Clemens, A. W. James, Fracture repair requires TrkA signaling by skeletal sensory nerves. *Journal of Clinical Investigation* **129**, 5137–5150 (2019).

15. B. G. Matthews, S. Novak, F. V. Sbrana, J. L. Funnell, Y. Cao, E. J. Buckels, D. Grcevic, I. Kalajzic, Heterogeneity of murine periosteum progenitors involved in fracture healing. *eLife* **10**, e58534 (2021).

16. S. Perrin, C.-A. Wotawa, V. Bretegnier, M. Luka, F. Coulpier, C. Masson, M. Ménager, C. Colnot, Single nuclei transcriptomics reveal the differentiation trajectories of periosteal skeletal/stem progenitor cells in bone regeneration (2024), doi:10.7554/eLife.92519.1.

17. N. van Gastel, S. Stegen, G. Eelen, S. Schoors, A. Carlier, V. W. Daniëls, N. Baryawno, D. Przybylski, M. Depypere, P.-J. Stiers, D. Lambrechts, R. Van Looveren, S. Torrekens, A. Sharda, P. Agostinis, D. Lambrechts, F. Maes, J. V. Swinnen, L. Geris, H. Van Oosterwyck, B. Thienpont, P. Carmeliet, D. T. Scadden, G. Carmeliet, Lipid availability determines fate of skeletal progenitor cells via SOX9. *Nature* **579**, 111–117 (2020).

18. J. Sales de Gauzy, F. Fitoussi, J.-L. Jouve, C. Karger, A. Badina, A.-C. Masquelet, Traumatic diaphyseal bone defects in children. *Orthopaedics & Traumatology: Surgery & Research* **98**, 220–226 (2012).

19. J. de la Croix Ndong, D. M. Stevens, G. Vignaux, S. Uppuganti, D. S. Perrien, X. Yang, J. S. Nyman, E. Harth, F. Elefteriou, Combined MEK Inhibition and BMP2 Treatment Promotes Osteoblast Differentiation and Bone Healing in *Nf1* $_{Osx}$ $^{-/-}$ Mice: RAS/ERK SIGNALING IN OSTEOPROGENITORS. *J Bone Miner Res* **30**, 55–63 (2015).

20. T. El Khassawna, D. Toben, M. Kolanczyk, K. Schmidt-Bleek, I. Koennecke, H. Schell, S. Mundlos, G. N. Duda, Deterioration of fracture healing in the mouse model of NF1 long bone dysplasia. *Bone* **51**, 651–660 (2012).

21. N. Kamiya, R. Yamaguchi, O. Aruwajoye, A. J. Kim, G. Kuroyanagi, M. Phipps, N. S. Adapala, J. Q. Feng, H. K. Kim, Targeted Disruption of *NF1* in Osteocytes Increases FGF23 and Osteoid With Osteomalacia-like Bone Phenotype: NF1 DISRUPTION IN OSTEOCYTES CAUSES A MINERALIZATION DEFECT. *J Bone Miner Res* **32**, 1716–1726 (2017).

22. R. Sharma, X. Wu, S. D. Rhodes, S. Chen, Y. He, J. Yuan, J. Li, X. Yang, X. Li, L. Jiang, E. T. Kim,

514 D. A. Stevenson, D. Viskochil, M. Xu, F.-C. Yang, Hyperactive Ras/MAPK signaling is critical for tibial
515 nonunion fracture in neurofibromin-deficient mice. *Human Molecular Genetics* **22**, 4818–4828 (2013).
516 23. W. Wang, J. S. Nyman, K. Ono, D. A. Stevenson, X. Yang, F. Elefteriou, Mice lacking Nf1 in
517 osteochondroprogenitor cells display skeletal dysplasia similar to patients with neurofibromatosis type
518 I. *Human Molecular Genetics* **20**, 3910–3924 (2011).
519 24. K. J. Radomska, F. Coulpier, A. Gresset, A. Schmitt, A. Debbiche, S. Lemoine, P. Wolkenstein, J.-
520 M. Vallat, P. Charnay, P. Topilko, Cellular Origin, Tumor Progression, and Pathogenic Mechanisms of
521 Cutaneous Neurofibromas Revealed by Mice with Nf1 Knockout in Boundary Cap Cells. *Cancer Discov*
522 **9**, 130–147 (2019).
523 25. A. Gresset, F. Coulpier, G. Gerschenfeld, A. Jourdon, G. Matesic, L. Richard, J.-M. Vallat, P.
524 Charnay, P. Topilko, Boundary Caps Give Rise to Neurogenic Stem Cells and Terminal Glia in the Skin.
525 *Stem Cell Reports* **5**, 278–290 (2015).
526 26. S. Ahsan, Y. Ge, M. A. Tainsky, Combinatorial therapeutic targeting of BMP2 and MEK-ERK
527 pathways in NF1-associated malignant peripheral nerve sheath tumors. *Oncotarget* **7**, 57171–57185
528 (2016).
529 27. E. Dombi, A. Baldwin, L. J. Marcus, M. J. Fisher, B. Weiss, A. Kim, P. Whitcomb, S. Martin, L. E.
530 Aschbacher-Smith, T. A. Rizvi, J. Wu, R. Ershler, P. Wolters, J. Therrien, J. Glod, J. B. Belasco, E.
531 Schorry, A. Brofferio, A. J. Starosta, A. Gillespie, A. L. Doyle, N. Ratner, B. C. Widemann, Activity of
532 Selumetinib in Neurofibromatosis Type 1-Related Plexiform Neurofibromas. *N Engl J Med* **375**, 2550–
533 2560 (2016).
534 28. D. Casey, S. Demko, A. Sinha, P. S. Mishra-Kalyani, Y.-L. Shen, S. Khasar, M. A. Goheer, W. S.
535 Helms, L. Pan, Y. Xu, J. Fan, R. Leong, J. Liu, Y. Yang, K. Windsor, M. Ou, O. Stephens, B. Oh, G. H.
536 Reaman, A. Nair, S. S. Shord, V. Bhatnagar, S. R. Daniels, S. Sickafuse, K. B. Goldberg, M. R. Theoret,
537 R. Pazdur, H. Singh, FDA Approval Summary: Selumetinib for Plexiform Neurofibroma. *Clin Cancer Res*
538 **27**, 4142–4146 (2021).
539 29. A. M. Gross, E. Dombi, P. L. Wolters, A. Baldwin, A. Dufek, K. Herrera, S. Martin, J. Derdak, K. S.
540 Heisey, P. M. Whitcomb, S. M. Steinberg, D. J. Venzon, M. J. Fisher, A. R. Kim, M. Bornhorst, B. D.
541 Weiss, J. O. Blakeley, M. A. Smith, B. C. Widemann, Long-Term Safety and Efficacy of Selumetinib in
542 Children with Neurofibromatosis Type 1 on a Phase 1/2 Trial for Inoperable Plexiform Neurofibromas.
543 *Neuro Oncol* , noad086 (2023).

30. G. S. Baht, P. Nadesan, D. Silkstone, B. A. Alman, Pharmacologically targeting beta-catenin for NF1 associated deficiencies in fracture repair. *Bone* **98**, 31–36 (2017).

31. N. Deo, T. L. Cheng, K. Mikulec, L. Peacock, D. G. Little, A. Schindeler, Improved union and bone strength in a mouse model of NF1 pseudarthrosis treated with recombinant human bone morphogenetic protein-2 and zoledronic acid: rhBMP-2 AND ZA FOR NF1 PSEUDARTHROSIS. *J. Orthop. Res.* (2017), doi:10.1002/jor.23672.

32. W. Wang, J. S. Nyman, H. E. Moss, G. Gutierrez, G. R. Mundy, X. Yang, F. Elefteriou, Local low-dose lovastatin delivery improves the bone-healing defect caused by Nf1 loss of function in osteoblasts. *J Bone Miner Res* **25**, 1658–1667 (2010).

33. J. Cai, S. Jacob, R. Kurupi, K. M. Dalton, C. Coon, P. Greninger, R. K. Egan, G. T. Stein, E. Murchie, J. McClanaghan, Y. Adachi, K. Hirade, M. Dozmorov, J. Glod, S. A. Boikos, H. Ebi, H. Hao, G. Caponigro, C. H. Benes, A. C. Faber, High-risk neuroblastoma with NF1 loss of function is targetable using SHP2 inhibition. *Cell Rep* **40**, 111095 (2022).

34. J. Wang, K. Pollard, A. N. Allen, T. Tomar, D. Pijnenburg, Z. Yao, F. J. Rodriguez, C. A. Pratilas, Combined Inhibition of SHP2 and MEK Is Effective in Models of NF1-Deficient Malignant Peripheral Nerve Sheath Tumors. *Cancer Res* **80**, 5367–5379 (2020).

35. A. P. W. Johnston, S. A. Yuzwa, M. J. Carr, N. Mahmud, M. A. Storer, M. P. Krause, K. Jones, S. Paul, D. R. Kaplan, F. D. Miller, Dedifferentiated Schwann Cell Precursors Secreting Paracrine Factors Are Required for Regeneration of the Mammalian Digit Tip. *Cell Stem Cell* **19**, 433–448 (2016).

36. V. Parfejevs, J. Debbache, O. Shakhova, S. M. Schaefer, M. Glausch, M. Wegner, U. Suter, U. Riekstina, S. Werner, L. Sommer, Injury-activated glial cells promote wound healing of the adult skin in mice. *Nat Commun* **9**, 236 (2018).

37. B. E. Bobick, W. M. Kulyk, MEK-ERK signaling plays diverse roles in the regulation of facial chondrogenesis. *Exp Cell Res* **312**, 1079–1092 (2006).

38. B. E. Bobick, W. M. Kulyk, The MEK-ERK signaling pathway is a negative regulator of cartilage-specific gene expression in embryonic limb mesenchyme. *J Biol Chem* **279**, 4588–4595 (2004).

39. J. Li, Z. Zhao, J. Liu, N. Huang, D. Long, J. Wang, X. Li, Y. Liu, MEK/ERK and p38 MAPK regulate chondrogenesis of rat bone marrow mesenchymal stem cells through delicate interaction with TGF-beta1/Smads pathway. *Cell Prolif* **43**, 333–343 (2010).

40. S. Murakami, M. Kan, W. L. McKeehan, B. de Crombrugghe, Up-regulation of the chondrogenic

574 Sox9 gene by fibroblast growth factors is mediated by the mitogen-activated protein kinase pathway.
575 *Proc Natl Acad Sci U S A* **97**, 1113–1118 (2000).
576 41. C. D. Oh, S. H. Chang, Y. M. Yoon, S. J. Lee, Y. S. Lee, S. S. Kang, J. S. Chun, Opposing role of
577 mitogen-activated protein kinase subtypes, erk-1/2 and p38, in the regulation of chondrogenesis of
578 mesenchymes. *J Biol Chem* **275**, 5613–5619 (2000).
579 42. A. D. Weston, R. A. S. Chandraratna, J. Torchia, T. M. Underhill, Requirement for RAR-mediated
580 gene repression in skeletal progenitor differentiation. *J Cell Biol* **158**, 39–51 (2002).
581 43. M. C. Harrisingh, E. Perez-Nadales, D. B. Parkinson, D. S. Malcolm, A. W. Mudge, A. C. Lloyd, The
582 Ras/Raf/ERK signalling pathway drives Schwann cell dedifferentiation. *EMBO J* **23**, 3061–3071 (2004).
583 44. I. Napoli, L. A. Noon, S. Ribeiro, A. P. Kerai, S. Parrinello, L. H. Rosenberg, M. J. Collins, M. C.
584 Harrisingh, I. J. White, A. Woodhoo, A. C. Lloyd, A central role for the ERK-signaling pathway in
585 controlling Schwann cell plasticity and peripheral nerve regeneration in vivo. *Neuron* **73**, 729–742
586 (2012).
587 45. I. Cervellini, J. Galino, N. Zhu, S. Allen, C. Birchmeier, D. L. Bennett, Sustained MAPK/ERK
588 Activation in Adult Schwann Cells Impairs Nerve Repair. *J Neurosci* **38**, 679–690 (2018).
589 46. A. P. W. Johnston, S. Naska, K. Jones, H. Jinno, D. R. Kaplan, F. D. Miller, Sox2-mediated regulation
590 of adult neural crest precursors and skin repair. *Stem Cell Reports* **1**, 38–45 (2013).
591 47. A. Badache, N. Muja, G. H. De Vries, Expression of Kit in neurofibromin-deficient human Schwann
592 cells: role in Schwann cell hyperplasia associated with type 1 neurofibromatosis. *Oncogene* **17**, 795–
593 800 (1998).
594 48. G. A. Mashour, N. Ratner, G. A. Khan, H. L. Wang, R. L. Martuza, A. Kurtz, The angiogenic factor
595 midkine is aberrantly expressed in NF1-deficient Schwann cells and is a mitogen for neurofibroma-
596 derived cells. *Oncogene* **20**, 97–105 (2001).
597 49. D. M. Patmore, S. Welch, P. C. Fulkerson, J. Wu, K. Choi, D. Eaves, J. J. Kordich, M. H. Collins, T.
598 P. Cripe, N. Ratner, *In Vivo* Regulation of TGF-β by R-Ras2 Revealed through Loss of the RasGAP
599 Protein NF1. *Cancer Research* **72**, 5317–5327 (2012).
600 50. J. El-Hoss, T. Cheng, E. C. Carpenter, K. Sullivan, N. Deo, K. Mikulec, D. G. Little, A. Schindeler, A
601 Combination of rhBMP-2 (Recombinant Human Bone Morphogenetic Protein-2) and MEK (MAP
602 Kinase/ERK Kinase) Inhibitor PD0325901 Increases Bone Formation in a Murine Model of
603 Neurofibromatosis Type I Pseudarthrosis. *The Journal of Bone and Joint Surgery* **96**, e117 (2014).

51. A. Julien, A. Kanagalingam, E. Martínez-Sarrà, J. Megret, M. Luka, M. Ménager, F. Relaix, C. Colnot, Direct contribution of skeletal muscle mesenchymal progenitors to bone repair. *Nature Communications* **12**, 2860 (2021).

52. A. C. Masquelet, F. Fitoussi, T. Begue, G. P. Muller, [Reconstruction of the long bones by the induced membrane and spongy autograft]. *Ann Chir Plast Esthet* **45**, 346–353 (2000).

53. M. Logan, J. F. Martin, A. Nagy, C. Lobe, E. N. Olson, C. J. Tabin, Expression of Cre recombinase in the developing mouse limb bud driven by aPrxl enhancer. *genesis* **33**, 77–80 (2002).

54. M. D. Muzumdar, B. Tasic, K. Miyamichi, L. Li, L. Luo, A global double-fluorescent Cre reporter mouse. *Genesis* **45**, 593–605 (2007).

55. L. Madisen, T. A. Zwingman, S. M. Sunkin, S. W. Oh, H. A. Zariwala, H. Gu, L. L. Ng, R. D. Palmiter, M. J. Hawrylycz, A. R. Jones, E. S. Lein, H. Zeng, A robust and high-throughput Cre reporting and characterization system for the whole mouse brain. *Nat Neurosci* **13**, 133–140 (2010).

56. Y. Zhu, M. I. Romero, P. Ghosh, Z. Ye, P. Charnay, E. J. Rushing, J. D. Marth, L. F. Parada, Ablation of NF1 function in neurons induces abnormal development of cerebral cortex and reactive gliosis in the brain. *Genes Dev* **15**, 859–876 (2001).

Acknowledgements

We thank A. Henry, A. Guigan and O. Pellé from the Flow Cytometry platforms of IMRB and Imagine Institute, L. Slimani and K. Henri from Life Imaging Facility of Paris Cité University (Plateforme Imagerie du Vivant “Micro-CT platform”), all the staff from the Imagine genomic core facility at Imagine Institute and N. Cagnard from Bioinformatics Platform at Imagine Institute for advice and technical assistance. We thank A. Julien, C. Goachet, M. Ethel, S. Berger, E. Tacu, E. Paniel, A. Heisler, and M. Mansour for technical assistance or advice.

Fundings

This work was supported by

Association Neurofibromatoses et Recklinghausen (C.C and B.P.), Osteosynthesis and Trauma Care Foundation (C.C. and St.P.), Agence Nationale de la Recherche-18-CE14-0033 and 21-CE18-007-01 (C.C, P.T. and B.P.), US Department of the Army NF220019 (C.C.), National Institutes of Health NIAMS R01 AR081671 (C.C. and Ralph Marcucio), and IMRB Cross team award (C.C. and P.T.). S. Perrin and O. Duchamp de Lageneste were supported by a PhD fellowship from Paris Cité University.

Author contributions

Si.P., C.C., P.T. and B.P. conceptualized and formulated the project. Si.P., Sa.P., I.L., V.B, O.D.d.L, N.P., O.R., M.L., F.C., C.M., T.M., and M.Z. performed experiments. St.P., P.W., S.H-R., K.R., P.T. and M.M. provided resources. Si.P. performed bioinformatic analyses. C.C. supervised the work. Si.P. generated the figures. Si.P. and C.C. wrote the original draft of the manuscript. P.T. and B.P reviewed and edited the manuscript.

Competing interests

The authors declare that they have no competing interests.

Data and materials availability

All data from this study are present in the paper or supplementary materials. Single-nuclei RNAseq and bulk RNAseq datasets generated for this study are deposited in GEO (GSE232516, GSE232517, GSE234071) and are publicly available.

Figures

Figure 1

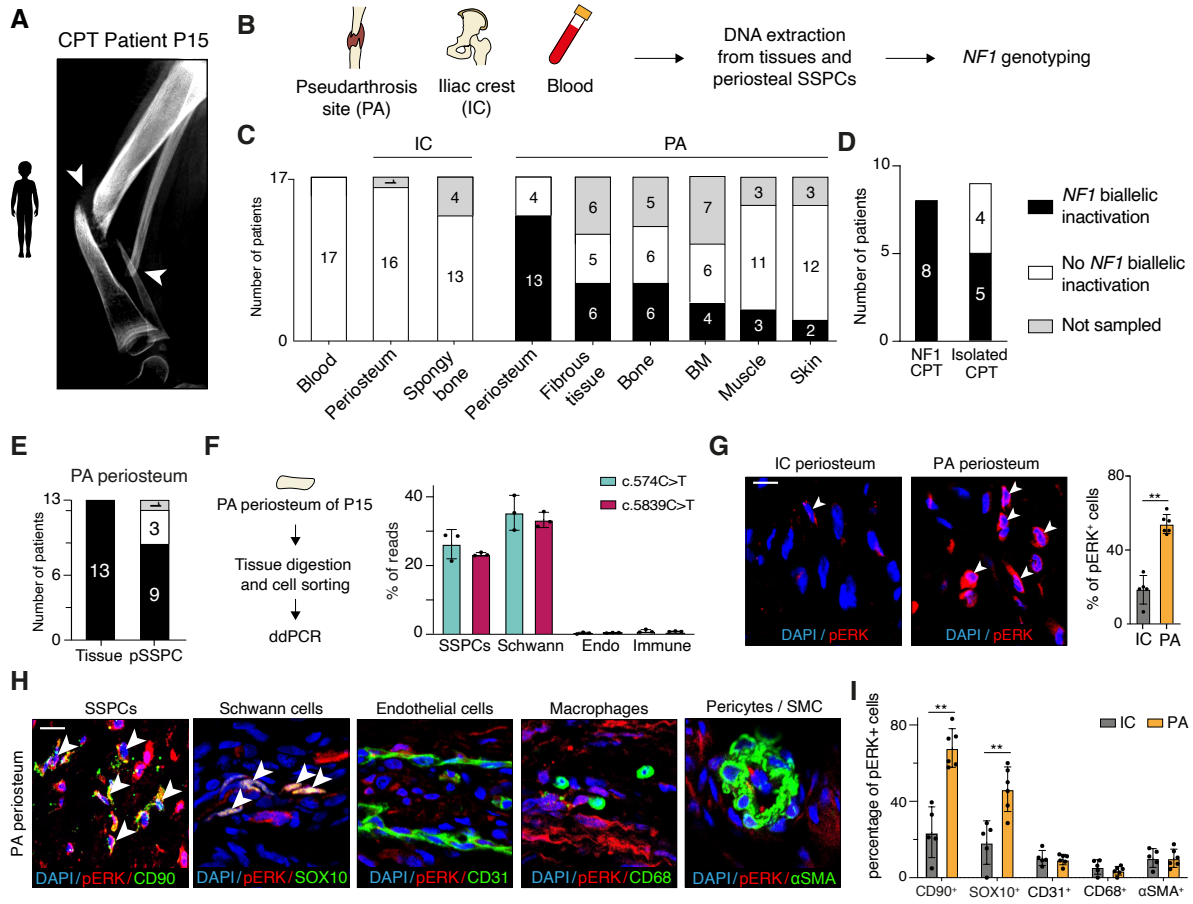

Figure 1: Schwann cells and SSPCs within periosteum harbor *NF1* biallelic inactivation in CPT

A. X-ray of the tibia and fibula pseudarthrosis (white arrows) of patient with CPT P15. **B.** Experimental design. DNA was extracted from tissues or periosteal SSPCs (pSSPCs) collected at the pseudarthrosis (PA) site and the iliac crest (IC), and from blood of patients with CPT undergoing surgery, and *NF1* targeted sequencing was performed. **C.** *NF1* genotyping of tissues from 17 patients with CPT shows the absence of *NF1* biallelic inactivation in blood and IC and the presence of *NF1* biallelic inactivation in the periosteum at PA site in 13/17 patients. *NF1* biallelic inactivation was also detected in 6/17 patients in fibrous tissue and bone, in 4/17 in bone marrow, in 3/17 in muscle, and in 2/17 in PA site skin. **D.** Number of patients with NF1-related CPT and isolated CPT carrying *NF1* biallelic inactivation. **E.** *NF1* genotyping of periosteum and SSPCs from PA site shows the presence of *NF1* biallelic inactivation in 9/13 patients. **F.** Left: experimental design. Cell populations were digested and sorted from PA periosteum of patient

P15 and the frequency of the 2 *NF1* point mutations (c.574C>T and c.5839C>T) was determined using droplet digital PCR (ddPCR). Right: Percentage of the 2 mutations in the different cell populations showing that Schwann cells and SSPCs carry both *NF1* hits, but not endothelial and immune cells. (n= 3 replicates). **G.** Phospho-ERK (pERK) immunofluorescence on periosteum sections showing number of pERK+ cells in the periosteum from PA site compared to the periosteum from IC (white arrows). Quantification of the percentage of pERK+ cells in the periosteum from PA and IC (n=5-6 patients per group). **H.** Co-immunofluorescence of pERK and CD90, SOX10, CD31, CD68 and αSMA on PA periosteum sections. **I.** Quantification of pERK+ cells in PA periosteum compared to IC periosteum (n= 5-6 patients per group). ** $p < 0.01$. BM: Bone marrow. Endo: endothelial cells. Scale bars: 50µm.

Figure 2

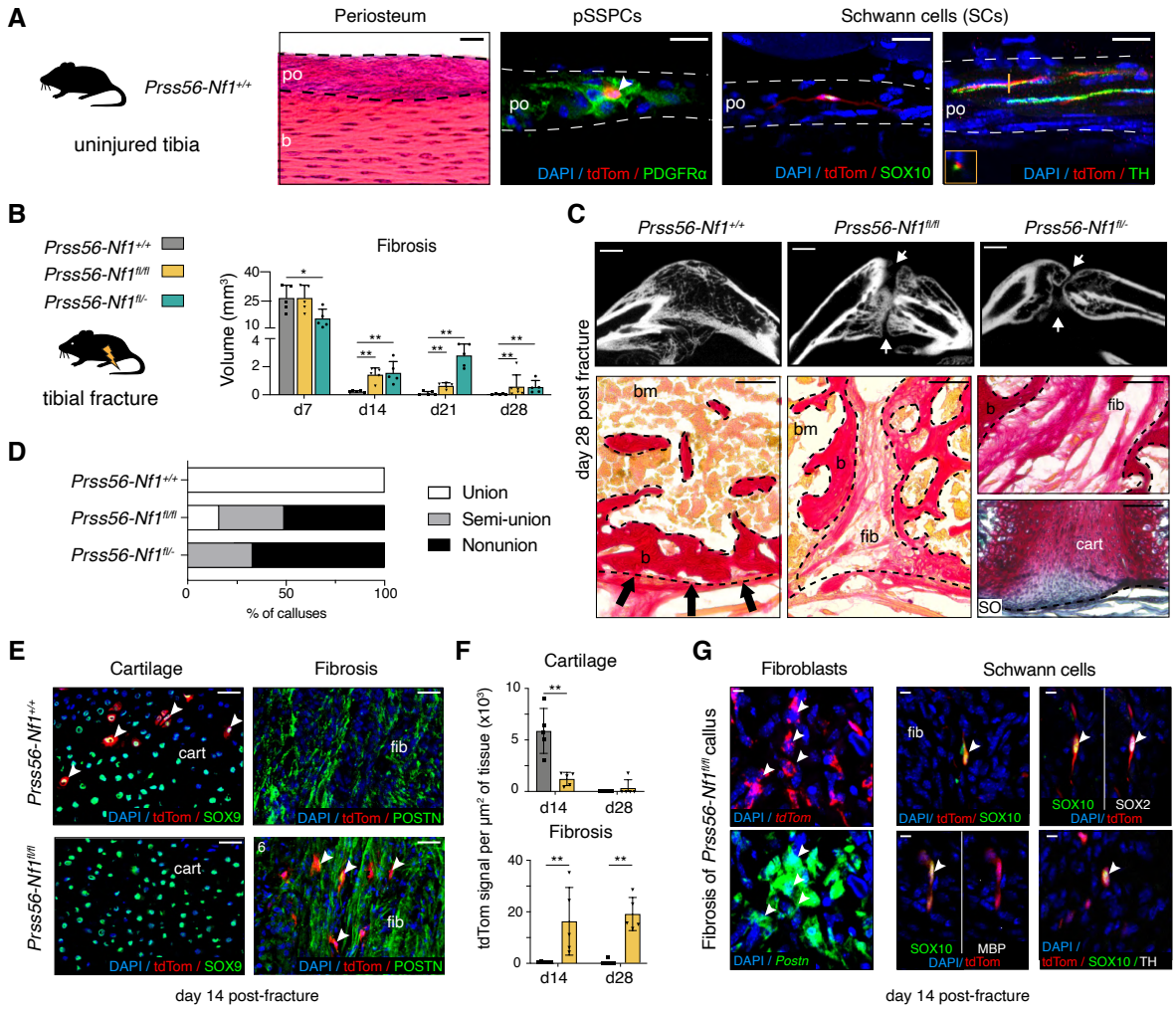

Figure 2: Tibial pseudarthrosis in mice lacking *Nf1* gene in boundary cap-derived pSSPCs and Schwann cells

A. Longitudinal sections of uninjured tibia periosteum (po) from 3-month-old *Prss56-Nf1*$^{+/+}$ mice stained with Hematoxylin-Eosin and immunofluorescence on adjacent sections showing tdTom+ periosteal skeletal stem/progenitor cells (pSSPCs) expressing PDGFRα and tdTom+ Schwann cells (SCs) expressing SOX10 along TH+ nerves (orange box: transverse imaging). **B.** Left: Experimental design of tibial fracture in *Prss56*^{Cre}*; R26*^{tdTom}*; Nf1*$^{+/+}$ (*Prss56-Nf1*$^{+/+}$) control, *Prss56*^{Cre}*; R26*^{tdTom}*; Nf1*$^{fl/fl}$ (*Prss56-Nf1*$^{fl/fl}$) and *Prss56*^{Cre}*; R26*^{tdTom}*; Nf1*$^{fl/-}$ (*Prss56-Nf1*$^{fl/-}$) mutant mice. Right: Histomorphometric quantification of the volume of callus fibrosis at days 7, 14, 21 and 28 post-fracture in *Prss56-Nf1*$^{+/+}$, *Prss56-Nf1*$^{fl/fl}$ and *Prss56-Nf1*$^{fl/-}$ mice (n=5-6 mice per group). **C.** Top: Representative microCT images of callus from *Prss56-Nf1*$^{+/+}$, *Prss56-Nf1*$^{fl/fl}$ and *Prss56-Nf1*$^{fl/-}$ mice at 28 days post-fracture, showing

absence of bone bridging in *Prss56-Nf1*$^{fl/fl}$ and *Prss56-Nf1*$^{fl/-}$ mutant mice (white arrows). Bottom, high magnification of callus periphery showing bone bridging (black arrows) in *Prss56-Nf1*$^{+/+}$ control mice, and fibrosis and unresorbed cartilage (red, Safranin'O (SO)) in *Prss56-Nf1*$^{fl/fl}$ and *Prss56-Nf1*$^{fl/-}$ mutant mice. **D.** Percentage of calluses from *Prss56-Nf1*$^{+/+}$, *Prss56-Nf1*$^{fl/fl}$ and *Prss56-Nf1*$^{fl/-}$ mice showing bone union (white), semi-union (grey), or nonunion (black) on microCT scan at day 28 post-fracture (n=6 mice per group). Bone union was significantly different between mutant and control mice (***, p=0.0067) but not between the mutant groups (p=0.52). **E.** Lineage tracing of Prss56-expressing Boundary Cap (BC)-derived tdTom+ cells (white arrowheads) in callus cartilage (labelled by SOX9) and fibrosis (labelled by POSTN) of *Prss56-Nf1*$^{+/+}$ and *Prss56-Nf1*$^{fl/fl}$ mice 14 days after tibial fracture. **F.** Quantification of tdTom+ signal in cartilage and fibrosis of *Prss56-Nf1*$^{+/+}$ and *Prss56-Nf1*$^{fl/fl}$ mice 14- and 28-days post-fracture (n=5 mice per group). **G.** RNAscope and immunofluorescence on callus sections of *Prss56-Nf1*$^{fl/fl}$ mice day 14 post-fracture show the presence of *Postn*-expressing tdTom+ fibroblasts and SOX10+tdTom+ SCs in fibrotic tissue. po: periosteum, b: bone, fib: fibrosis, cart: cartilage, bm: bone marrow, SO: Safranin'O. p-value: * $p < 0.05$, ** $p < 0.01$. Scale bars: Panel A: 25µm. Panel C-microCT: 1mm. Panel E/C-histology: 100µm. Panel G: 10µm.

Figure 3

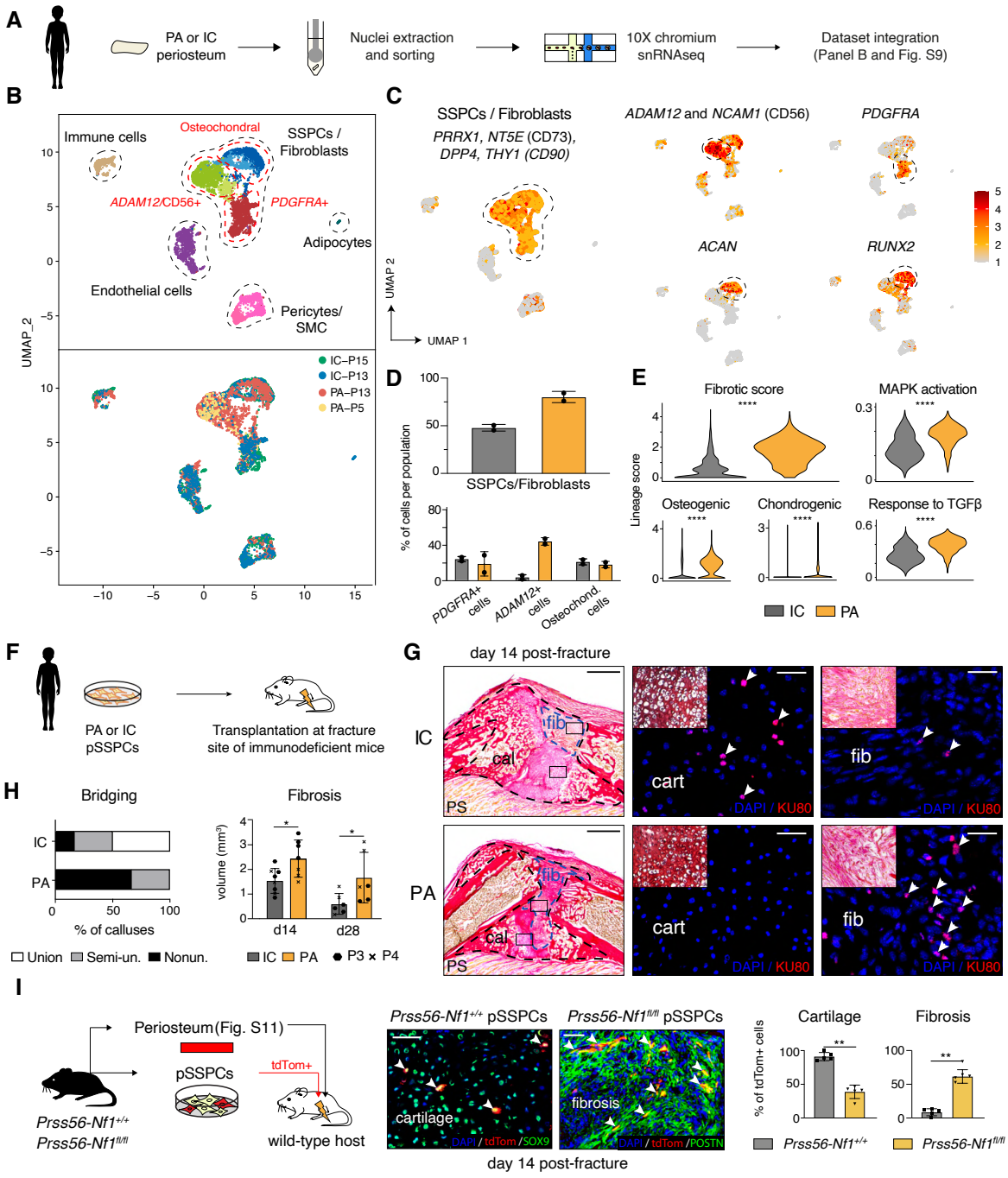

Figure 3: Fibrotic fate of *NF1*-deficient periosteal SSPCs in patients with CPT and *Prss56-Nf1 KO* mice

A. Experimental design. Nuclei were extracted from PA or IC periosteum, sorted, and processed for single-nuclei RNAseq. The datasets were integrated for analyses. **B.** UMAP projection of color-coded clustering (top) and sampling (bottom) of the integration of the datasets of IC periosteum from P15 (IC-

P15, green), IC periosteum from P13 (IC-P13, blue), PA periosteum from P13 (PA-P13, red) and PA periosteum from P5 (PA-P5, yellow). **C.** Feature plots of the SSPC/fibroblast lineage score and *ADAM12/NCAM1 (*Neural Cell Adhesion Molecule 1*)*, *PDGFRA*, *ACAN,* and *RUNX2* gene expression. **D.** Percentage of cells from PA and IC samples in SSPC/fibroblast populations and in *ADAM12*+, *PDGFRA*+, and osteochondral clusters. **E.** Violin plots of the fibrotic, osteogenic, chondrogenic, MAPK activation, and cellular response to TGFβ lineage score in IC and PA. **F.** Experimental design. PA or IC pSSPCs from patients P3 and P4 were transplanted at the fracture site of immunodeficient mice. **G.** Representative callus sections stained with Picrosirius (PS). High magnification of cartilage stained with Safranin'O and fibrosis stained with PS and immunofluorescence of the human KU80 protein at day 14 post-fracture showing that IC pSSPC-derived cells are located mostly in cartilage while PA pSSPC-derived cells are located in fibrosis (white arrow). **H.** Left: Percentage of callus grafted with PA or IC pSSPCs showing union, semi-union, and nonunion at day 28 post-fracture. Right: Volume of fibrosis in day 14 and 28 post-fracture callus of immunodeficient mice grafted with human pSSPCs from IC and PA (n=6-8 mice per group). **I.** Left: Experimental design. Periosteum or cultured tdTom^{+} periosteal skeletal stem/progenitor cells (pSSPCs) were isolated from *Prss56-Nf1*$^{+/+}$ or *Prss56-Nf1*$^{fl/fl}$ mice and transplanted at the fracture site of wild-type hosts. Middle: Representative images of the contribution of grafted tdTom+ cells (white arrows) showing cells from *Prss56-Nf1*$^{+/+}$ mice detected in cartilage (labelled by SOX9) and cells from *Prss56-Nf1*$^{fl/fl}$ mice detected in fibrosis (labelled by POSTN). Right: Percentage of grafted tdTom+ cells in cartilage and fibrosis (n=5 mice per group). SMC: smooth muscle cells, cal: callus, fib: fibrosis, cart: cartilage. p-value: * $p < 0.05$, ** $p < 0.01$, **** $p < 0.0001$. Scale bars: Panel G: Low magnification: 1mm. High magnification: 100µm. Panel I: 100µm.

Figure 4

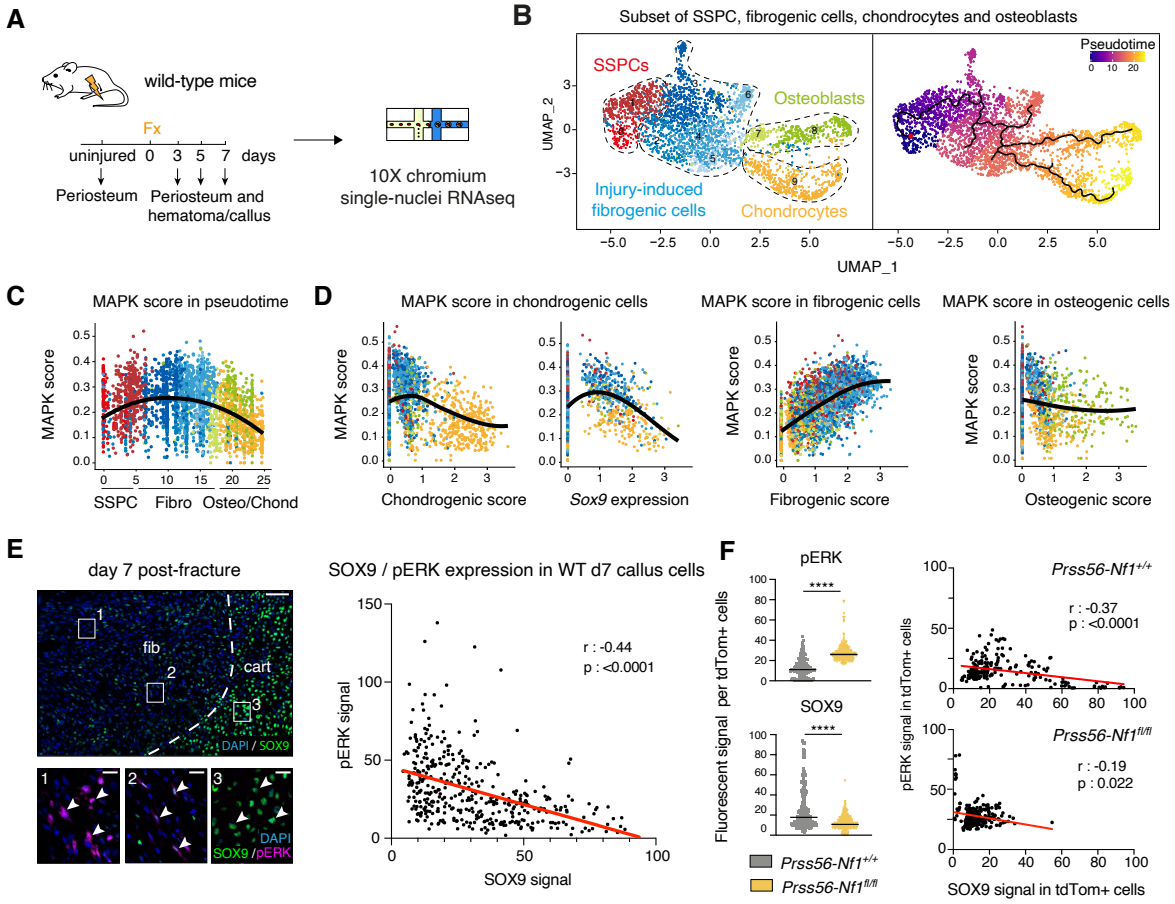

729

730 **Figure 4: Overactivation of MAPK pathway causes fibrotic differentiation of *Nf1*-deficient**
731 **pSSPCs**

732 **A.** Experimental design of single nuclei RNAseq (snRNAseq) experiment. Nuclei were isolated from
733 uninjured periosteum, or periosteum and hematoma of wild type mice at days 3, 5, and 7 post- tibial
734 fracture, sorted, and processed for snRNAseq. **B.** UMAP projection of clustering and monocle
735 pseudotime trajectory of the subset of SSPCs, injury-induced fibrogenic cells, osteoblasts, and
736 chondrocytes from integrated uninjured, day 3, day 5, and day 7 post-fracture samples. The four
737 populations are delimited by black dashed lines. **C.** Scatter plot of MAPK score along pseudotime. **D.**
738 Scatter plots of MAPK score along chondrogenic lineage score, *Sox9* expression, fibrogenic, and
739 osteogenic lineage scores. **E.** Immunofluorescence of SOX9 and phospho-ERK (pERK) in day 7 post-
740 fracture callus section of wild type (WT) mice. Quantification and correlation of SOX9 and pERK signal
741 per cell (red line) (n = 397 cells from 8 callus sections of 4 mice). Scale bars: low magnification, 150µm;

high magnification, 25μm. **F.** Left: Quantification of SOX9 and pERK fluorescent signal per tdTom+ cells in day 7 post-fracture callus of *Prss56-Nf1*$^{+/+}$ and *Prss56-Nf1*$^{fl/fl}$ mice. Right: Correlation analysis of pERK and SOX9 signals in tdTom+ cells in *Prss56-Nf1*$^{+/+}$ (top) and *Prss56-Nf1*$^{fl/fl}$ (bottom) mice (n = 209 to 238 cells from 9 sections of 3 mice per group). cart: cartilage, fib: fibrosis. ****: $p < 0.0001$.

Figure 5

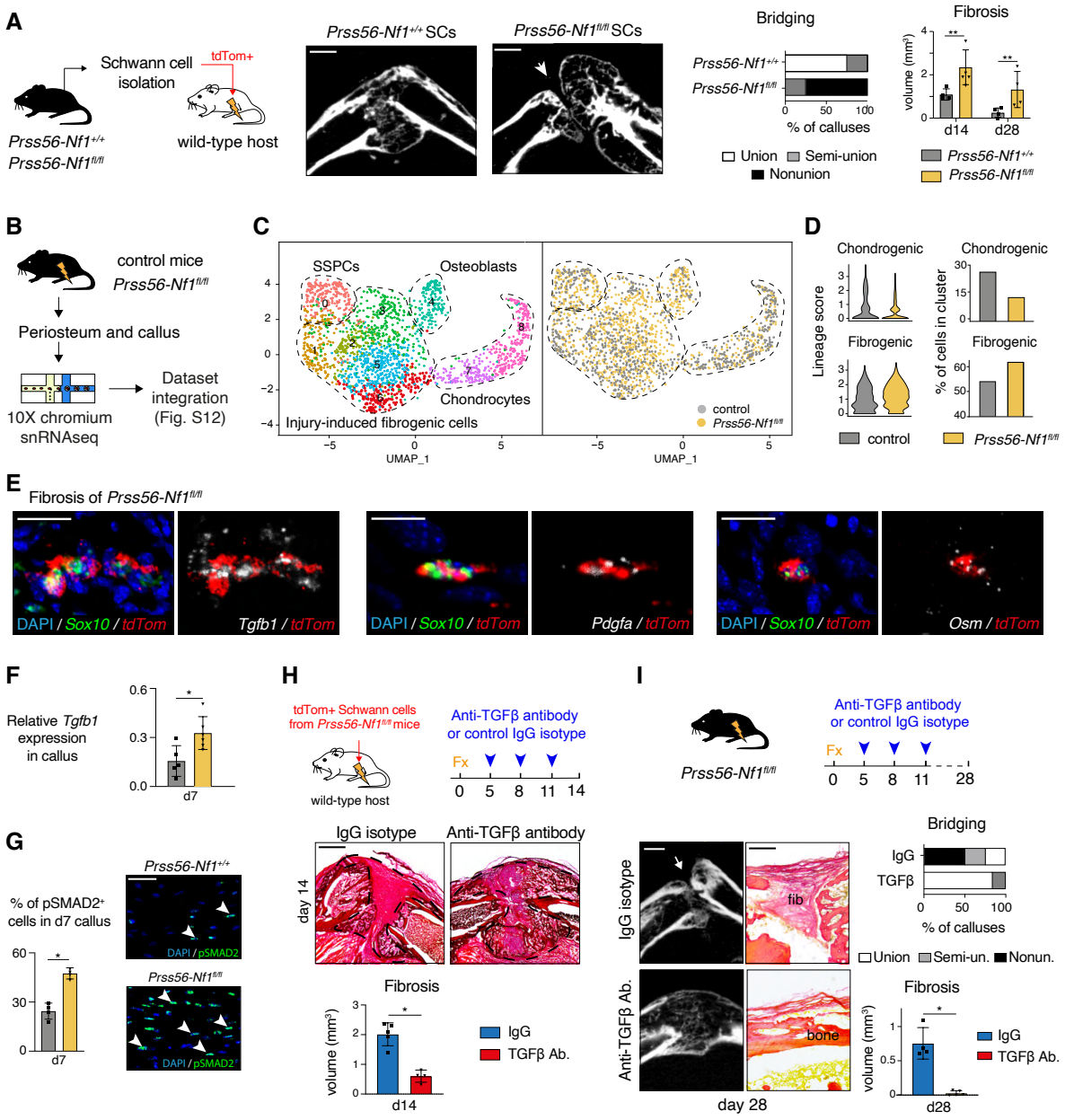

Figure 5: Pro-fibrotic effect of *Nf1*-deficient Schwann cells in fibrous nonunion

A. Left: Experimental design. tdTom+ Schwann cells (SCs) were isolated from *Prss56-Nf1*$^{+/+}$ or *Prss56-Nf1*$^{fl/fl}$ mice and transplanted at the fracture site of wild-type hosts. Middle: MicroCT images of 28 days post-fracture calluses of wild-type mice grafted with SCs from *Prss56-Nf1*$^{+/+}$ or *Prss56-Nf1*$^{fl/fl}$ mice, showing absence of bridging in mice grafted with *Nf1*-deficient SCs (white arrow). Right: Percentage of day 28 post-fracture calluses showing union, semi-union, or nonunion. Volume of callus fibrosis at 14 and 28 days post-fracture (n=4-5 mice per group). **B.** Experimental design. Nuclei were isolated from periosteum and hematoma at day 7 post-fracture of control or *Prss56-Nf1*$^{fl/fl}$ mice and processed for

snRNAseq. Datasets were integrated. **C.** UMAP projection of SSPC, injury-induced fibrogenic, chondrogenic, and osteogenic cell subsets from the integrated day 7 post-fracture control and *Prss56-Nf1$^{fl/fl}$* datasets. **D.** Violon plot of chondrogenic and fibrogenic lineage scores per dataset. Percentage of cells per cluster. **E.** RNAscope experiment on day 7 post-fracture callus from *Prss56-Nf1$^{fl/fl}$* mice shows the expression of *Tgfb1, Pdgfa*, and *Osm* by *Sox10-, tdTom*-expressing Schwann cells in callus fibrosis. **F.** Relative expression of *Tgfb1* in day 7 post-fracture callus of *Prss56-Nf1$^{+/+}$* or *Prss56-Nf1$^{fl/fl}$* mice (n=5 mice per group). **G.** Percentage of phospho-SMAD2 positive (pSMAD2+) cells in the day 7 post-fracture callus of *Prss56-Nf1$^{+/+}$* or *Prss56-Nf1$^{fl/fl}$* mice (n=4 mice per group). Representative pSMAD2 immunofluorescence of *Prss56-Nf1$^{+/+}$* or *Prss56-Nf1$^{fl/fl}$* callus. **H.** Top: Experimental design. Wild-type mice grafted with tdTom+ Schwann cells from *Prss56-Nf1$^{fl/fl}$* mice were treated with blocking TGFβ antibody or IgG1 control isotype at days 5, 8, and 11 post-fracture. Middle: Picrosirius staining of fracture calluses at 14 days post-fracture. Bottom: Volume of callus fibrosis (n=4-5 mice per group). **I.** Top: Experimental design. *Prss56-Nf1$^{fl/fl}$* mice were treated with blocking TGFβ antibody or IgG1control isotype at days 5, 8, and 11 post-fracture. Middle: MicroCT images of callus of *Prss56-Nf1$^{fl/fl}$* mice treated with IgG1 isotype control or TGFβ blocking antibody at 28 days post-fracture. High magnification of the callus periphery stained with Picrosirius. Bottom left: percentage of day 28 post-fracture calluses showing union (white), semi-union (grey) or nonunion (black) on microCT scan. Bottom right: Volume of callus fibrosis of *Prss56-Nf1$^{fl/fl}$* mice treated with blocking TGFβ antibody or IgG1 isotype control at 28 days post-fracture. (n=4-5 mice per group). p-value: * $p < 0.05$, ** $p < 0.01$. Scale bars: Panel A/H 1mm. Panel E: 10µm. Panel G 50µm, panel I: Low magnification: 1mm, High magnification: 250 µm.

Figure 6

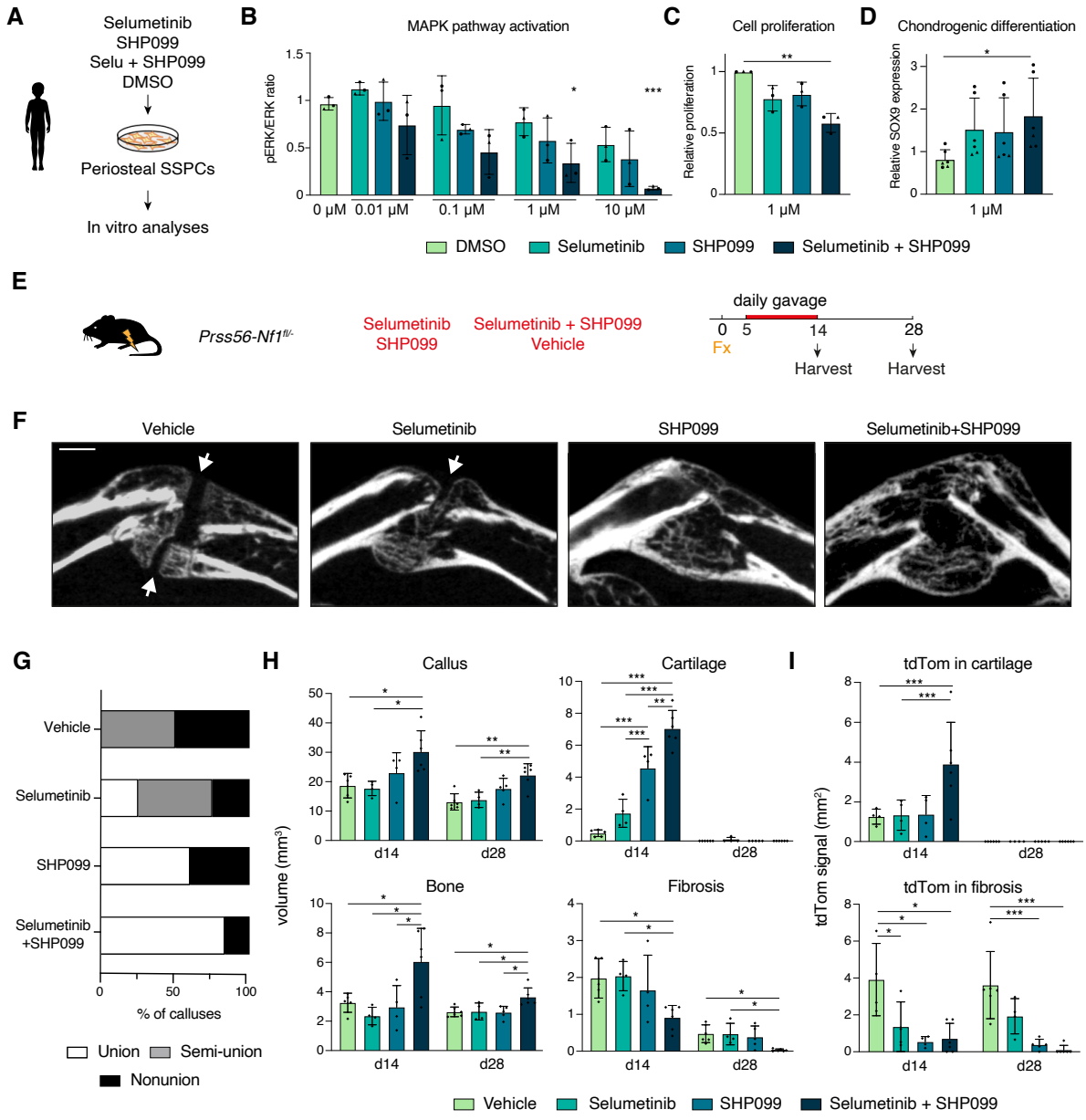

Figure 6: Combined MEK and SHP2 inhibition prevents fibrous nonunion in *Prss56-Nf1* KO mice

A. Experimental design. Periosteal SSPCs from PA site of patients with CPT were treated with MEK inhibitor (selumetinib), SHP2 inhibitor (SHP099), MEK and SHP2 inhibitors (selumetinib and SHP099), or vehicle (DMSO) for in vitro analyses. **B.** MAPK pathway activation in pSSPCs from PA site treated with selumetinib, SHP099, selumetinib and SHP099, or DMSO measured by the pERK/ERK ratio on Western blot. Statistical significance was determined compared to DMSO control (n=3 patients). **C.** Reduced in vitro proliferation of pSSPCs from PA site treated with combined selumetinib and SHP099

(n=3 patients). **D.** Increased in vitro chondrogenic differentiation measured by *SOX9* expression of pSSPCs from PA site treated with combined selumetinib and SHP099 (n=3 patients in duplicates). **E.** Experimental design. *Prss56-Nf1*$^{fl/-}$ mice were treated by oral gavage with selumetinib, SHP099, selumetinib and SHP099, or vehicle from days 5 to 14 post-fracture. **F.** Representative microCT images of callus from *Prss56-Nf1*$^{fl/-}$ mice at 28 days post-fracture, with bone bridging indicated by white arrows. **G.** Percentage of calluses from treated and control *Prss56-Nf1*$^{fl/-}$ mice showing bone union (white), semi-union (grey), or nonunion (black) on microCT scan at day 28 post-fracture (n=4-6 mice per group). **H.** Volume of callus, cartilage, bone, and fibrosis at days 14 and 28 post-fracture in treated and control *Prss56-Nf1*$^{fl/-}$ mice (n=4-6 mice per group). **I.** Surface of tdTom signal in cartilage and fibrosis of day 14 and 28 callus from treated and control *Prss56-Nf1*$^{fl/-}$ mice. Scale bars: 1mm. p-value: * $p < 0.05$, ** $p < 0.01$, *** $p < 0.001$.